Chinese Chemical Letters 37 (2026) 111399

Contents lists available at ScienceDirect

Chinese Chemical Letters

journal homepage: www.elsevier.com/locate/cclet

Dual-gated delivery of melittin combined with moderate photothermal treatment using NIR-responsive Pd nanosheets for enhanced cancer immunotherapy

Dongsheng Zhang[a,1], Tingting Wang[a,1], Cheng-Ao Li[d,1], Yi Tang[b], Fangyang Wang[b], Qiang Wang[b], Hongqing Li[b], Xun Zhang[a], Duo Sun[b], Yueying Zhang[b], Jiang Ming[c], Xiao Chen[b,*], Xiaolan Chen[c,*], Jingchao Li[b,*], Xinhui Su[a,*]

[a] PET Center, Department of Nuclear Medicine, The First Affiliated Hospital, Zhejiang University School of Medicine, Hangzhou 310003, China
[b] Department of Nuclear Medicine, Daping Hospital, Army Medical University, Chongqing 400042, China
[c] State Key Laboratory for Physical Chemistry of Solid Surfaces, Collaborative Innovation Center of Chemistry for Energy Materials, and Engineering Research Center for Nano-Preparation Technology of Fujian Province, College of Chemistry and Chemical Engineering Xiamen University, Xiamen 361005, China
[d] State Key Laboratory of Silicon and Advanced Semiconductor Materials, Institute for Composites Science Innovation, School of Materials Science and Engineering, Zhejiang University, Hangzhou 310058, China

ARTICLE INFO

Article history:
Received 6 March 2025
Revised 27 May 2025
Accepted 29 May 2025
Available online 29 May 2025

Keywords:
Melittin
Pd nanosheets
Drug delivery
Moderate photothermal therapy
Immunotherapy

ABSTRACT

Immunotherapy has emerged as a promising strategy for combating tumor metastasis and recurrence, however, its efficacy is often hampered by the immunosuppressive tumor microenvironment (TME). The integration of nanomedicine-based photothermal therapy (PTT) with immunotherapy offers great potential to reshape the immune landscape, thereby enhancing immune responses and therapeutic outcomes. Nevertheless, conventional hyperthermia may induce heat-related damage and excessive inflammation in normal tissues. To address this challenge, we developed a novel therapeutic platform that combines tumor-specific delivery of melittin (MLT) with mild PTT using two-dimensional palladium nanosheets (Pd NSs). This approach allows for selective accumulation of MLT at tumor sites *via* the enhanced permeability and retention (EPR) effect and TME-responsive release, thereby maximizing antitumor efficacy while minimizing off-target toxicity. The resulting nanocomposite, MLT@Pd@PEG, exhibits excellent biocompatibility and efficient photothermal conversion under 808 nm laser irradiation. The acidic pH and localized heat in the TME synergistically trigger the controlled release of MLT, which disrupts cancer cell membranes and promotes tumor cell apoptosis. Moreover, this treatment facilitates the release of tumor-associated antigens and danger-associated molecular patterns (DAMPs), thereby activating cytotoxic T lymphocytes and natural killer (NK) cells. *In vivo* studies demonstrate that the combination of immune checkpoint blockade and MLT@Pd@PEG not only eradicates primary and distant tumors in bilateral tumor-bearing mouse models but also prevents tumor recurrence and metastasis by inducing durable immune memory. This comprehensive strategy integrating precise MLT delivery with mild PTT holds significant promise for advancing next-generation cancer immunotherapy.

© 2026 Published by Elsevier B.V. on behalf of Chinese Chemical Society and Institute of Materia Medica, Chinese Academy of Medical Sciences.

Immunotherapy, a non-invasive strategy that leverages the innate immune system to recognize and eliminate cancer cells, has revolutionized cancer treatment in clinical settings [1,2]. Unlike traditional therapies such as surgery, radiotherapy, or chemotherapy, which directly target tumor cells, immunotherapy enhances or modulates immune responses to achieve long-lasting antitumor effects [3]. Despite its remarkable clinical success, the therapeutic efficacy of immunotherapy is often hindered by immune evasion, tumor heterogeneity, delivery barriers, and the risk of immune-related adverse events stemming from uncontrolled immune activation [4,5].

Melittin (MLT), a cationic host defense peptide derived from bee venom, exhibits potent immunomodulatory and antitumor properties. It facilitates the release of tumor-associated antigens (TAAs), activates cytotoxic T lymphocytes and natural killer (NK) cells, and stimulates the secretion of proinflammatory cytokines, thereby potentiating antitumor immunity [6–9]. Additionally, MLT reprograms

* Corresponding authors.
E-mail addresses: xiaochen229@tmmu.edu.cn (X. Chen), chenxl@xmu.edu.cn (X. Chen), lijc@tmmu.edu.cn (J. Li), suxinhui@zju.edu.cn (X. Su).
[1] These authors contributed equally to this work.

https://doi.org/10.1016/j.cclet.2025.111399
1001-8417/© 2026 Published by Elsevier B.V. on behalf of Chinese Chemical Society and Institute of Materia Medica, Chinese Academy of Medical Sciences.

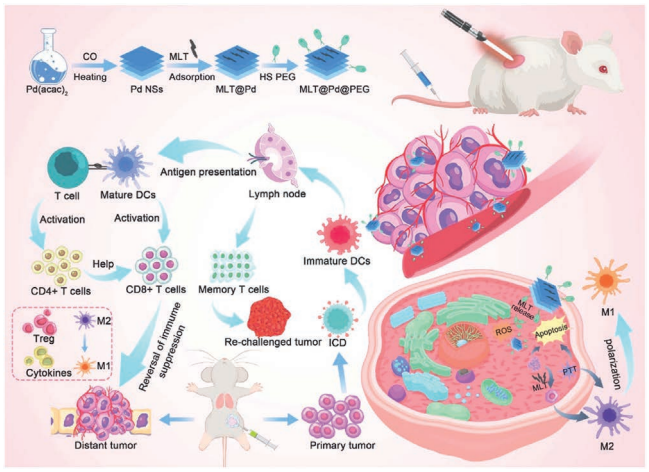
tumor-associated macrophages (TAMs) toward an immunostimulatory M1 phenotype, helping to remodel the immunosuppressive tumor microenvironment (TME) [10,11]. Mechanistically, MLT induces cancer cell necrosis or apoptosis by disrupting the cell membrane *via* pore formation [12,13]. Moreover, its mitochondria-targeting ability leads to mitochondrial dysfunction and oxidative stress through reactive oxygen species (ROS) generation, further suppressing autophagy and promoting cell death [14,15]. However, its clinical translation remains limited due to issues such as narrow therapeutic window, hemolytic activity, rapid clearance, and systemic toxicity [16].

Photothermal therapy (PTT) has emerged as a promising complementary strategy owing to its precision, efficiency, and minimal invasiveness. Nanoparticle-assisted PTT not only ablates tumors but also induces immunogenic cell death (ICD), thereby releasing TAAs and damage-associated molecular patterns (DAMPs) to stimulate systemic antitumor immunity [17–20]. Nevertheless, the immunosuppressive nature of the TME continues to compromise therapeutic outcomes [21,22]. To address this, combining PTT with immunoadjuvants or immunotherapies has shown potential in amplifying immune responses, inhibiting tumor recurrence, and improving treatment efficacy [23,24]. Notably, moderate PTT can elicit immune responses while avoiding the detrimental effects of high-temperature hyperthermia, thereby preserving the functionality of co-delivered biomolecules [25,26].

Among various nanomaterials, two-dimensional palladium nanosheets (Pd NSs) have attracted considerable interest due to their high photothermal conversion efficiency, favorable biocompatibility, and intrinsic EPR-based tumor-targeting ability [27–30]. Our previous studies revealed that Pd NSs with an edge length of ~41 nm exhibited a photothermal conversion efficiency of approximately 27.6% under near-infrared (NIR) irradiation [31]. When accumulated at tumor sites, Pd NSs effectively ablate tumors and facilitate localized drug release under mild photothermal conditions [32–34]. However, the instability of thermally sensitive therapeutic agents like MLT under hyperthermic conditions poses a challenge for effective delivery and retention of bioactivity. Mild PTT has recently gained traction as it not only enhances drug release but also reprograms the TME and induces pyroptosis, thereby boosting the efficacy of gene therapy, radiotherapy, and immunotherapy through hypoxia alleviation and immune stimulation [35–38]. Intriguingly, recent studies have shown that mild photothermal stimulation upregulates PD-L1 expression on cancer cells, thereby enhancing the effectiveness of immune checkpoint blockade (ICB) therapy [37–39].

In light of these insights, we developed a multifunctional nanoplatform MLT@Pd@PEG *via* a straightforward self-assembly method to enable targeted MLT delivery combined with mild PTT. This formulation exhibits high MLT loading capacity and excellent stability under physiological conditions, effectively mitigating MLT-induced hemolysis and off-target toxicity. The pH/temperature-responsive release mechanism ensures the selective release of MLT in the TME, thereby achieving efficient tumor cell apoptosis and growth inhibition. Furthermore, MLT@Pd@PEG induces ICD and promotes M2-to-M1 macrophage polarization, enhancing cytokine secretion (*e.g.*, interleukin-6 (IL-6), interferon-γ (IFN-γ), tumor necrosis factor-α (TNF-α)) and upregulating PD-L1 expression to potentiate ICB therapy. Most importantly, this strategy triggers long-term immune memory, providing sustained protection against tumor recurrence. Together, our MLT@Pd@PEG system represents a promising approach to overcoming the limitations of conventional immunotherapy and advancing cancer photothermal-immunotherapy (Scheme 1).

Pd NSs were synthesized *via* the reduction of $Pd(acac)_2$ under a carbon monoxide atmosphere, as previously reported [27]. Subsequently, MLT was electrostatically grafted onto the surface of Pd NSs at room temperature under stirring to form MLT@Pd nanocomplexes. These were then surface-functionalized with thiol-terminated polyethylene glycol (mPEG-SH) to yield the final MLT@Pd@PEG nanocomplexes. Transmission electron microscopy (TEM) analysis revealed that the resulting MLT@Pd@PEG nanocomplexes were monodisperse, with an average diameter of ~30 nm (Fig. 1a). High-angle annular dark-field scanning TEM (HAADF-STEM) imaging, coupled with elemental mapping, confirmed the



Scheme 1. Schematic illustration showing the preparation of MLT@Pd@PEG nanoformulations with the ability to controllably deliver MLT and induce moderate PTT for enhanced tumor immunotherapy.

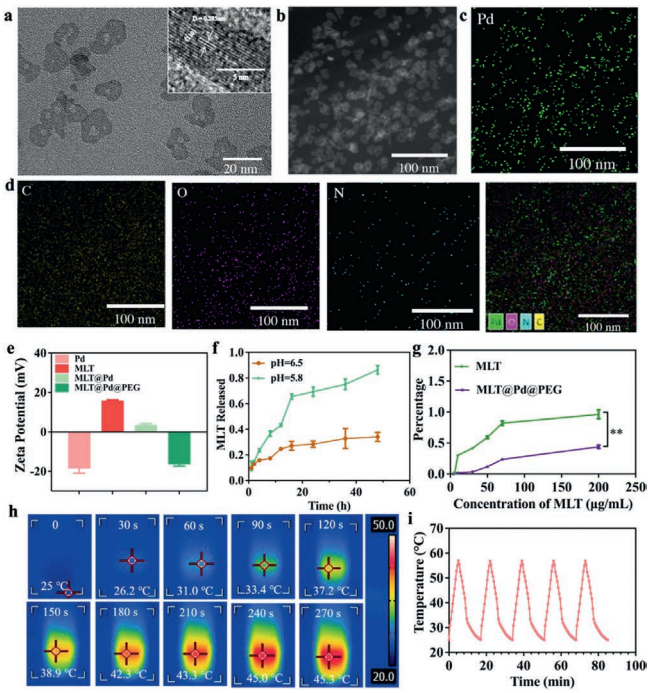


Fig. 1. Structure and property characterizations of the MLT@Pd@PEG nanocomplexes. (a) TEM image of MLT@Pd@PEG nanocomplexes. The inset shown the HR-TEM images of MLT@Pd@PEG nanocomplexes. (b) HAADF-TEM image of MLT@Pd@PEG nanocomplexes. (c, d) Corresponding element (including C, O, N, and Pd elements) mapping of MLT@Pd@PEG nanocomplexes. (e) The zeta potential of the as-synthesized Pd, MLT, MLT@Pd, and MLT@Pd@PEG nanocomplexes. (f) Cumulative MLT release profile of the MLT@Pd@PEG nanocomplexes in different conditions at each time point. (g) Corresponding hemolysis rates of the red blood cell (RBC) count. Data are presented as mean ± standard deviation (SD) ($n = 3$). $^{**}P < 0.01$. (h) Infrared thermal images of MLT@Pd@PEG nanocomplexes (200 μg/mL) in 500 μL PBS under laser irradiation (808 nm, 0.5 W/cm^2). (i) The photothermal stability of MLT@Pd@PEG nanocomplexes.

uniform distribution of C, N, O, and Pd elements throughout the nanostructures (Figs. 1b–d). Zeta potential measurements illustrated distinct surface charges at each modification step. Both free MLT and MLT@Pd nanocomplexes exhibited positive surface charges, while Pd NSs and MLT@Pd@PEG nanocomplexes displayed negative zeta potentials, suggesting successful MLT loading and PEGylation (Fig. 1e). Dynamic light scattering (DLS) further revealed slight increases in hydrodynamic size after sequential MLT and PEG modification, corroborating effective surface engineering (Fig. S1 in Supporting information). The pH-responsive drug release behavior of MLT@Pd@PEG was evaluated in buffers of different pH values. At pH 5.8, approximately 60 % of MLT was released within 8 h, and over 80 % was released after 12 h, indicating sustained and pH-sensitive release behavior under mildly acidic conditions mimicking the TME (Fig. 1f). To confirm the stepwise fabrication process, ultraviolet-visible (UV–vis) spectroscopy absorption spectra of Pd NSs, MLT, MLT@Pd, and MLT@Pd@PEG were recorded (Fig. S2 in Supporting information). Pd NSs exhibited broad absorption due to surface plasmon resonance. After MLT loading, a slight red shift in MLT's characteristic peak was observed, suggesting π–metal interactions. PEGylation led to a reduction in absorbance intensity and broadening of the spectra, indicative of improved colloidal stability.

Hemolysis assays demonstrated that Pd NSs significantly mitigated the hemolytic activity of free MLT, which typically disrupts red blood cell membranes (Fig. 1g and Fig. S3 in Supporting information). The colloidal stability of MLT@Pd@PEG was systematically evaluated in phosphate-buffered saline (PBS), DMEM, and fetal bovine serum (FBS) using UV–vis, DLS, and zeta potential analyses. Over 72 h, no noticeable spectral changes or aggregation were observed (Fig. S4 in Supporting information). The nanocomplexes maintained stable hydrodynamic diameters (~80–90 nm) and moderately negative surface charges (–18.2 ~ –12.9 mV) across all media (Tables S1 and S2 in Supporting information), indicating excellent dispersion and physicochemical stability suitable for biological applications.

The photothermal performance of MLT@Pd@PEG nanocomplexes was evaluated under NIR laser irradiation (808 nm, 0.2 W/cm^2). Aqueous dispersions of MLT@Pd@PEG at varying concentrations (50–200 μg/mL) exhibited rapid temperature increases upon NIR exposure, with a 100 μg/mL solution reaching 46.4 °C within 600 s (Figs. S6a and b in Supporting information). Infrared thermal imaging further confirmed their effective photothermal conversion (Fig. 1h). Importantly, the nanocomplexes maintained stable photothermal performance over four heating–cooling cycles (Fig. 1i), indicating excellent photothermal durability. Furthermore, MLT release from MLT@Pd@PEG nanocomplexes was significantly accelerated upon NIR irradiation and decreased rapidly once the laser was turned off (Fig. S7 in Supporting information), confirming the feasibility of controlled release *via* mild photothermal heating.

Building upon the favorable properties of the nanocomplex, we further investigated the cytotoxicity of MLT@Pd@PEG nanocomplexes in 4T1 cells. Prior to evaluating their cytotoxic and therapeutic efficacy, cellular uptake at various incubation time points was assessed using confocal laser scanning microscopy (CLSM) and flow cytometry. For fluorescence tracking, the nanocomplexes were labeled with Cy5.5. As shown in Fig. 2a and Fig. S8 (Supporting information), cellular internalization of MLT@Pd-Cy5.5@PEG increased over time, with substantial uptake observed after 6 h of incubation. The *in vitro* cytotoxicity of MLT@Pd@PEG nanocomplexes was determined using a cell counting kit-8 (CCK-8) assay. As shown in Figs. 2b and c, all groups displayed dose- and time-dependent cytotoxicity. Notably, MLT@Pd exhibited a lower half maximal inhibitory concentration (IC_{50}) (12.82 ± 0.69 μg/mL) compared to MLT@Pd@PEG (21.79 ± 0.30 μg/mL), likely due to PEG shielding. Moreover, NIR laser irradiation significantly enhanced the cytotoxicity of MLT@Pd@PEG, as evidenced by decreased cell

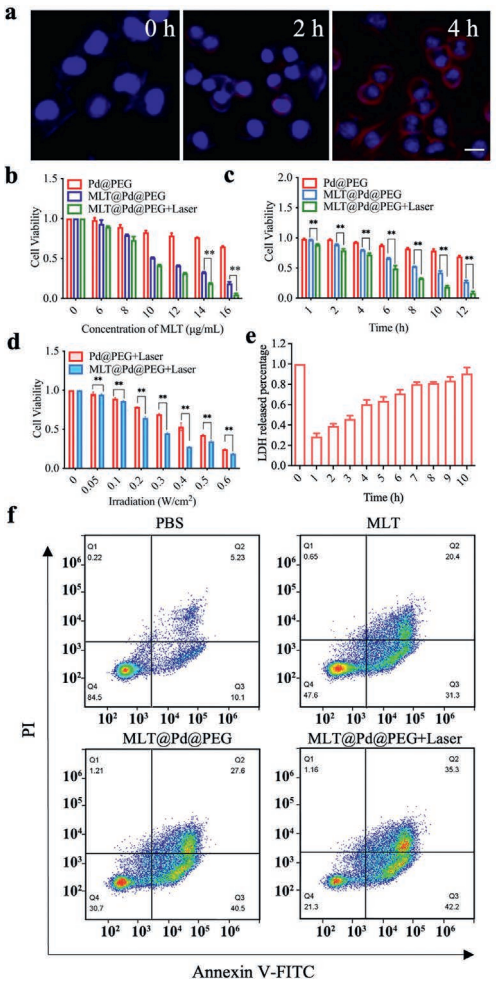


Fig. 2. *In vitro* synergistic antitumor performance of MLT@Pd@PEG nanocomplexes in 4T1 cells. (a) Confocal images of 4T1 cells after 0, 1, and 4 h incubation with MLT@Pd-Cy5.5@PEG nanocomplexes were labeled by red fluorescence and cell nuclei were stained with 2-(4-amidinophenyl)-6-indolecarbamidine dihydrochloride (DAPI). Scale bar: 50 μm. (b) Viability of 4T1 cells treated with various materials. (c) Viability of 4T1 cells treated with Pd@PEG and MLT@Pd@PEG nanocomplexes for different time. (d) Viabilities of 4T1 cells with different treatments. (e) The release of LDH from 4T1 cells after co-incubated with MLT@Pd@PEG nanocomplexes at different time points. (f) Flow cytometry analysis of 4T1 cell apoptosis from cells after different treatments. Data are presented as mean ± SD ($n = 3$). $^{**}P < 0.01$.

viability (Figs. 2d and f), which declined further with prolonged irradiation: 87.5 % viability at 5 min and 79.3 % at 10 min. These results indicate a robust photothermal effect, confirmed by the substantial temperature rise upon NIR exposure (Fig. S9a in Supporting information). To evaluate biocompatibility, human normal liver cells (L02) were incubated with various concentrations of MLT@Pd@PEG for 12 h. As shown in Fig. S9b (Supporting information), cell viability remained high (>91.2 %) at ~12 μg/mL, indicating negligible toxicity at therapeutic doses.

Cell apoptosis morphology was examined by CLSM and flow cytometry following nanoparticle treatment. 4T1 cells were stained with calcein AM and PI to distinguish live (green fluorescence) and dead (red fluorescence) cells. As shown in Fig. S10 (Supporting information), the MLT@Pd@PEG + laser group displayed significantly more red fluorescence than the MLT@Pd@PEG or saline groups, indicating a synergistic effect of photothermal and chemotherapeutic mechanisms. ICD, marked by the release of DAMPs (*e.g.*, surface-exposed calreticulin (CRT), extracellular high mobility group box-1 protein (HMGB1), and ATP), was next evaluated (Fig. S11 in Supporting information). Enzyme-linked immunosorbent assay (ELISA)

results (Fig. S11a) showed significantly increased HMGB1 secretion in the MLT@Pd@PEG group *versus* PBS and Pd@PEG groups, with further enhancement upon NIR irradiation. CRT exposure (Fig. S11b) and extracellular ATP release (Fig. S11c) also increased significantly post-treatment, indicating robust ICD induction. The release of MLT under NIR likely enhanced these effects.

To further confirm MLT-mediated membrane damage, CLSM was used to observe 4T1 cell membranes. As shown in Fig. S12 (Supporting information), free MLT disrupted membrane integrity more than MLT@Pd@PEG, though the latter still induced partial membrane compromise. MLT acts *via* pore formation, causing leakage of cytosolic contents such as lactate dehydrogenase (LDH). LDH release increased over time with MLT@Pd@PEG exposure (Fig. 2e), corroborating its membrane-disruptive activity. Lysosomal escape was assessed by CLSM (Fig. S13 in Supporting information), revealing MLT@Pd@PEG escaped lysosomes over time post-internalization. This was likely due to MLT's lipid-lytic activity within lysosomes, resulting in membrane rupture. ROS generation, assessed *via* DCFH-DA staining (Fig. S14 in Supporting information), was highest in the MLT@Pd@PEG group. ROS overproduction disrupted mitochondrial membrane potential, promoted cytochrome c release, and triggered caspase activation-key steps in apoptosis (Fig. S15 in Supporting information). Intracellular pH changes were measured using BCECF-AM, showing increased acidity in MLT@Pd@PEG-treated cells, likely a downstream effect of MLT action. JC-1 dye was used to assess mitochondrial membrane potential (Fig. S16 in Supporting information), which was reduced in MLT@Pd@PEG-treated cells, particularly after NIR irradiation, suggesting MLT-induced mitochondrial dysfunction amplified by hyperthermia.

Finally, we investigated the immunomodulatory effects of MLT@Pd@PEG on the TME. TAMs contribute to immunosuppression, with the M2 phenotype supporting tumor progression. MLT has been shown to repolarize M2 TAMs to the M1 phenotype. Our results confirmed that MLT downregulated M2 marker CD206 in IL-4-induced macrophages (Fig. S16), indicating successful reprogramming and potential reversal of the immunosuppressive TME).

Encouraged by the promising *in vitro* results, we further evaluated the pharmacokinetics, biodistribution, real-time imaging, and antitumor efficacy of MLT@Pd@PEG nanocomplexes *in vivo*. A 4T1 tumor-bearing mouse model was established *via* subcutaneous injection of 4T1 cells into female BALB/c mice. All animal experiments were performed according to a protocol approved by the Animal Experimental Ethical Inspection of the First Affiliated Hospital, Zhejiang University School of Medicine (approval No. 2023–428). Prior to therapy, the tumor-targeting capability of MLT@Pd@PEG was investigated using fluorescence imaging. Following intravenous injection of MLT@Pd-Cy5.5@PEG, fluorescence imaging revealed significant tumor accumulation after 12 h, with peak fluorescence observed at 48 h post-injection, attributed to prolonged blood circulation and the enhanced permeability and retention (EPR) effect (Fig. 3a). *Ex vivo* imaging of harvested major organs and tumors at 48 h further confirmed the selective accumulation in tumor tissues (Fig. S18 in Supporting information).

Photothermal conversion efficacy *in vivo* was validated using an infrared thermal imaging camera. Upon 808 nm laser irradiation (0.3 W/cm^2) for 5 min at 6 h post-injection, the tumor temperature rapidly rose to 45.5 °C, demonstrating efficient photothermal heating (Fig. S19 in Supporting information). To evaluate the therapeutic efficacy, mice were divided into six groups: (1) PBS, (2) PD-L1, (3) Pd@PEG, (4) MLT@Pd@PEG, (5) MLT@Pd@PEG + PD-L1, and (6) MLT@Pd@PEG + PD-L1 + laser. The nanocomplexes were intravenously administered three times every other day, and PTT was applied 12 h after each injection. Tumor volume analysis showed that MLT@Pd@PEG significantly suppressed tumor growth compared to the PBS and Pd@PEG groups, owing to the

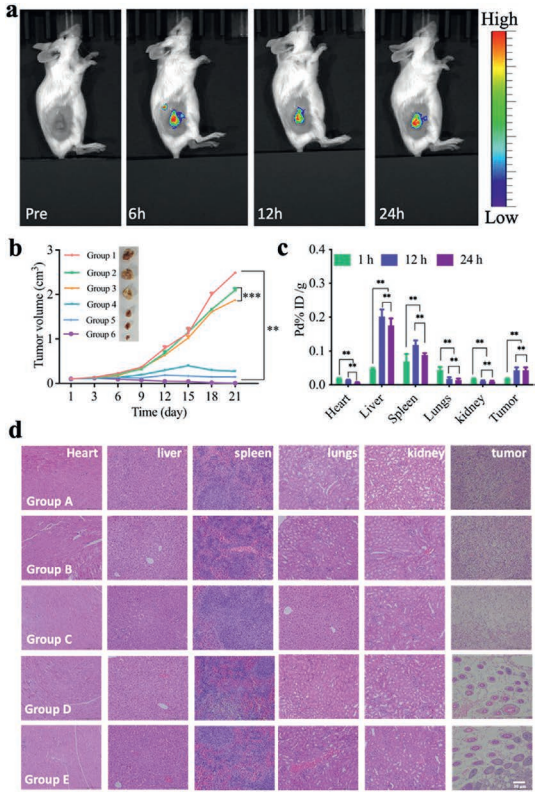


Fig. 3. *In vivo* antitumor efficacy and biodistribution of MLT@Pd@PEG nanocomplexes. Group 1: PBS; Group 2: anti-PD-L1; Group 3: Pd@PEG; Group 4: MLT@Pd@PEG; Group 5: MLT@Pd@PEG + anti-PD-L1; Group 6: MLT@Pd@PEG + anti-PD-L1 + laser. (a) *In vivo* fluorescence imaging of 4T1 tumor-bearing mice at different time points post-intravenous injection of MLT@Pd-Cy5.5@PEG nanocomplexes. (b) Tumor volume growth curves over 21 days and representative photographs of treated mice and excised tumors on day 21 ($n = 5$). (c) Quantitative analysis of nanocomplex accumulation in major organs and tumor tissues at different time points ($n = 3$). (d) H&E staining images of dissected major organs (heart, liver, spleen, lung, kidney) and tumor tissue of 4T1 tumor-bearing mice after various treatments by intravenous administration. Scale bar: 50 μm. Data are presented as mean ± SD. $^{**}P < 0.01$, $^{***}P < 0.001$.

membrane-disrupting activity of MLT. Notably, the group receiving MLT@Pd@PEG + PD-L1 + laser exhibited the most substantial tumor inhibition, confirming the synergistic effect of PTT and immunotherapy (Fig. 3B and Fig. S20 in Supporting information). No notable body weight changes were observed during the treatments (Fig. S21 in Supporting information), indicating minimal systemic toxicity.

ICP-MS analysis revealed markedly higher Pd ion accumulation in tumor tissues compared to other organs, confirming the tumor-targeting ability of MLT@Pd@PEG and its prolonged circulation (Fig. 3c). The elevated Pd levels in tumors over time implied a favorable EPR effect and microenvironment-triggered retention. Hematoxylin and eosin (H&E) staining of major organs indicated no histopathological abnormalities (Fig. 3d). Blood biochemical analysis showed a slight increase in white blood cell count, likely due to acute foreign body response induced by MLT@Pd@PEG, yet all parameters remained within normal physiological ranges (Fig. S22 in Supporting information), demonstrating good biocompatibility. Cytokine profiling by ELISA revealed elevated levels of IL-6, IL-12, TNF-α, and IFN-γ, especially in the MLT@Pd@PEG + PD-L1 + laser group, suggesting robust immune activation. Meanwhile, IL-10 expression was suppressed, indicating a reduction in immunosuppressive signaling and a favorable immunostimulatory profile (Fig. S23 in Supporting information). Furthermore, PD-L1 immunofluorescence staining confirmed upregulation of PD-L1 ex-

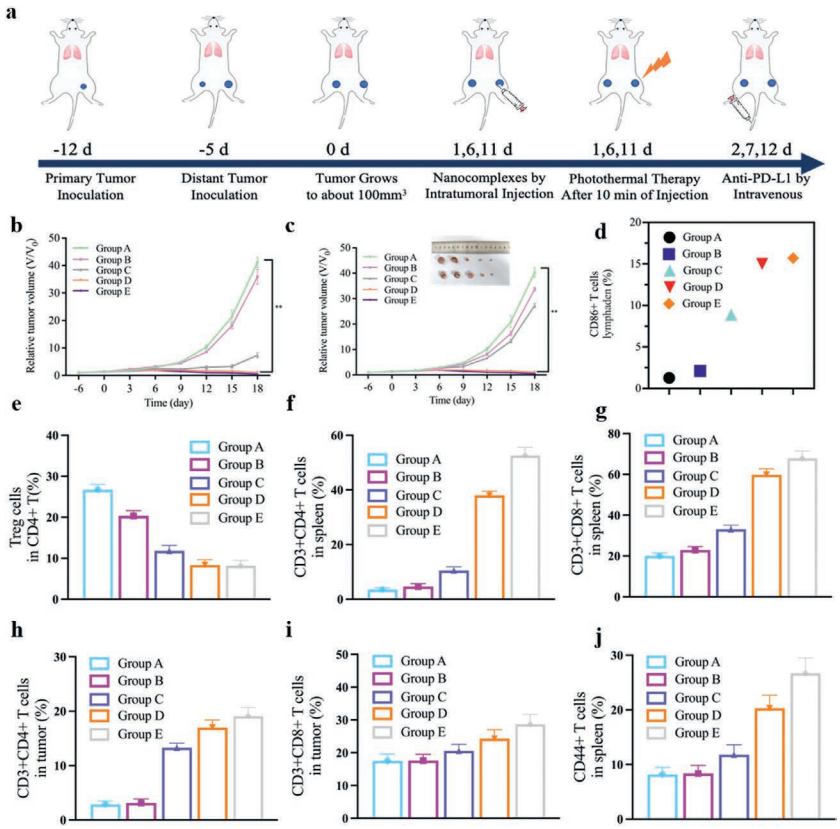


Fig. 4. *In vivo* evaluation of antitumor immune responses induced by MLT@Pd@PEG nanocomplexes in a bilateral 4T1 tumor model. Group A: Saline; Group B: Pd@PEG; Group C: MLT@Pd@PEG; Group D: MLT@Pd@PEG + anti-PD-L1; Group E: MLT@Pd@PEG + anti-PD-L1 + laser. (a) Schematic illustration of the experimental design for assessing therapeutic efficacy and immune activation in bilateral 4T1 tumor-bearing BALB/c mice. (b, c) Tumor growth curves of the primary (b) and distant (c) tumors following various treatments. (d) Flow cytometric analysis of mature dendritic cells ($CD11c^+CD86^+$) in the tumor-draining lymph nodes after treatment. (e) Quantitative analysis of $Foxp3^+$ Treg cells in primary tumors from different treatment groups *via* flow cytometry. (f, g) Quantitative analysis of $CD4^+$ (f) and $CD8^+$ (g) T cells in spleen from different treatment groups *via* flow cytometry. (h, i) Quantitative analysis of $CD4^+$ (h) and $CD8^+$ (i) T cells in primary tumors from different treatment groups *via* flow cytometry. (j) Quantitative analysis of mouse memory T cells in spleen from different treatment groups *via* flow cytometry. Data are presented as mean ± SD ($n = 3$). $^{**}P < 0.01$.

pression in tumor tissues following mild photothermal treatment (Fig. S24 in Supporting information), highlighting the role of moderate PTT in enhancing tumor immunogenicity.

Building on the encouraging intravenous results, we further explored the synergistic effect of MLT@Pd@PEG and ICB for bilateral tumor inhibition. Bilateral tumor models were established on both flanks of the mice, representing primary and distant (abscopal) tumors. The treatment schedule is illustrated in Fig. 4a. Mice were grouped as follows: (A) saline, (B) Pd@PEG, (C) MLT@Pd@PEG, (D) MLT@Pd@PEG + anti-PD-L1, and (E) MLT@Pd@PEG + anti-PD-L1 + laser. Each group received intratumoral injections every five days, repeated three times. Tumor growth was significantly inhibited in the MLT@Pd@PEG + anti-PD-L1 + laser group for both primary and abscopal tumors (Figs. 4b and c, Fig. S25 in Supporting information). This enhanced effect is partially attributed to moderate PTT-induced upregulation of PD-L1, which increased the intratumoral accumulation of anti-PD-L1 (Fig. 4d). In contrast, without laser or anti-PD-L1, the inhibition was limited to primary tumors, with distant tumors showing minimal response.

Mechanistically, MLT@Pd@PEG triggered ICD, promoting tumor antigen release and dendritic cell (DC) activation. Flow cytometry of tumor-draining lymph nodes showed a marked increase in mature DCs ($CD11c^+CD86^+$) after treatment, particularly in the MLT@Pd@PEG + anti-PD-L1 + laser group (50.1 %), compared to 13.6 % in the PBS group (Fig. 4e and Fig. S26 in Supporting information). Tumor-infiltrating Tregs ($CD4^+Foxp3^+$) were significantly reduced after treatment, alleviating immune suppression. The proportion of Tregs among $CD4^+$ T cells dropped from 26.7 % in the PBS group to 8.18 % in the combination group (Figs. 4f and g, Fig. S27 in Supporting information). Further, analysis of $CD4^+$ and $CD8^+$ T cells showed elevated infiltration in spleens and tumors, especially in the MLT@Pd@PEG + anti-PD-L1 + laser group (Figs. 4h and i, Figs. S28 and S29 in Supporting information), indicating potent systemic immune activation. Importantly, memory T cells ($CD3^+CD8^+CD62L-CD44^+$) were also increased, demonstrating long-term immune memory against tumor recurrence (Fig. 4j, Fig. S30 in Supporting information). Cytokine assays showed that IL-6, IL-12, TNF-α, and IFN-γ levels followed the trend: MLT@Pd@PEG + anti-PD-L1 + laser > MLT@Pd@PEG + anti-PD-L1 > MLT@Pd@PEG > saline (Fig. S31 in Supporting information), reinforcing the synergistic immunomodulatory effect.

In summary, we developed a multifunctional nanoplatform based on Pd NSs for targeted MLT delivery, enabling synergistic photothermal and immunotherapy. The MLT@Pd@PEG nanocomplex exhibited excellent biocompatibility, efficient NIR photothermal conversion, and tumor-targeted accumulation. Upon irradiation, the nanocomplex induced localized hyperthermia, dual-gated MLT release, and potent tumor cell ablation. Importantly, this strategy triggered ICD and promoted dendritic cell maturation, leading to robust activation of cytotoxic and memory T cells. When combined with anti-PD-L1 therapy, MLT@Pd@PEG effectively reshaped the immunosuppressive TME, upregulated PD-L1 expression, and enhanced immunotherapeutic efficacy. This resulted in significant inhibition of both primary and abscopal tumors, prevention of metastasis, and induction of long-term immune memory. This work provides a promising approach for

combinational nanomedicine-based cancer immunotherapy, offering a potential pathway to improve clinical outcomes with minimal systemic toxicity.

Declaration of competing interest

The authors declare that they have no known competing financial interests or personal relationships that could have appeared to influence the work reported in this paper.

CRediT authorship contribution statement

Dongsheng Zhang: Writing – review & editing, Writing – original draft, Validation, Resources, Methodology, Investigation, Data curation. **Tingting Wang:** Writing – review & editing, Writing – original draft, Visualization, Software, Investigation, Data curation. **Cheng-Ao Li:** Writing – review & editing, Writing – original draft, Resources, Methodology, Investigation, Data curation. **Yi Tang:** Writing – original draft, Validation, Resources, Investigation, Data curation. **Fangyang Wang:** Visualization, Software, Resources, Investigation, Formal analysis. **Qiang Wang:** Validation, Software, Methodology, Investigation, Data curation. **Hongqing Li:** Validation, Resources, Methodology, Investigation. **Xun Zhang:** Validation, Software, Investigation, Formal analysis. **Duo Sun:** Visualization, Software, Investigation. **Yueying Zhang:** Visualization, Validation, Investigation. **Jiang Ming:** Validation, Resources, Formal analysis. **Xiao Chen:** Writing – review & editing, Writing – original draft, Supervision, Investigation, Data curation, Conceptualization. **Xiaolan Chen:** Writing – review & editing, Writing – original draft, Supervision, Resources, Methodology, Conceptualization. **Jingchao Li:** Writing – review & editing, Writing – original draft, Supervision, Resources, Funding acquisition, Conceptualization. **Xinhui Su:** Writing – review & editing, Writing – original draft, Supervision, Resources, Project administration, Funding acquisition, Conceptualization.

Acknowledgments

This work was supported by the National Natural Science Foundation of China (Nos. 82071965, 12405399); National Key Research and Development Program of China (No. 2023YFF0716000); and Major plan of Jointly Constructed project by the Science and Technology Department of the State Administration of Traditional Chinese Medicine and the Zhejiang Provincial Administration of Traditional Chinese Medicine (No. GZY-ZJ-KJ-24025).

Supplementary materials

Supplementary material associated with this article can be found, in the online version, at doi:10.1016/j.cclet.2025.111399.

References

[1] Z. Li, X. Lai, S. Fu, L. Ren, H. Cai, Adv. Sci. 9 (2022) 2201734.
[2] R. Guo, S. Wang, L. Zhao, et al., Biomaterials 282 (2022) 121425.
[3] Q. Jiang, Y. Liu, R. Guo, et al., Biomaterials 192 (2019) 292–308.
[4] M. Kciuk, E.B. Yahya, M.M.I. Mohamed, et al., Cancers 15 (2023) 3298.
[5] R. Rui, L. Zhou, S. He, Front. Immunol. 14 (2023) 1212476.
[6] T. Nie, Y. Fang, R. Zhang, et al., Bioact. Mater. 47 (2025) 51–63.
[7] S.Y. Han, Z.X. Zhao, J. Wu, Mil. Med. Res. 11 (2024) 12.
[8] T. Nie, H. Liu, Z. Fang, et al., ACS Nano 17 (2023) 10925–10937.
[9] S. Han, J. Wu, Bioact. Mater. 17 (2022) 300–319.
[10] A. Bahreyni, H. Liu, Y. Mohamud, et al., BMC Med. 21 (2023) 193.
[11] R. Chen, J. Yang, M. Wu, et al., Adv. Mater. 35 (2023) 2304123.
[12] R. Ye, Y. Zheng, Y. Chen, et al., ACS Appl. Mater. Interfaces 13 (2021) 55902–55912.
[13] J. Zhou, C. Wan, J. Cheng, et al., ACS Appl. Mater. Interfaces 13 (2021) 17158–17173.
[14] X. Li, Z. Li, Y.Q. Meng, et al., Redox Rep. 28 (2023) 2284517.
[15] H. Wang, J. Li, Z. Wang, et al., Biomaterials 269 (2021) 120609.
[16] L. Zhu, J. Liu, M. Qiu, et al., Biomaterials 288 (2022) 121711.
[17] C. Xu, K. Pu, Chem. Soc. Rev. 50 (2021) 1111–1137.
[18] L. Xie, J. Li, G. Wang, et al., J. Am. Chem. Soc. 144 (2022) 787–797.
[19] Y. Li, K. Zhang, Y. Wu, et al., Small 18 (2022) 2107461.
[20] S. Tang, L. Zhou, H. He, et al., Biomaterials 288 (2022) 121706.
[21] Y. Qiu, Z. Wu, Y. Chen, et al., Adv. Sci. 10 (2023) 2300878.
[22] Q. Li, X. Liu, C. Yan, et al., Small 19 (2023) 2206211.
[23] X. Yin, Y. Cheng, Y. Feng, et al., Adv. Drug Deliv. Rev. 189 (2022) 114483.
[24] B. Ma, A. Bianco, Small 17 (2021) 2102557.
[25] Y. Li, F. Huang, P.J. Stang, S. Yin, Acc. Chem. Res. 57 (2024) 1174–1187.
[26] D. Xu, Y. Li, S. Yin, F. Huang, Chem. Soc. Rev. 53 (2024) 3167–3204.
[27] M. Jiang, M. Yan, J. Ye, et al., Coord. Chem. Rev. 506 (2024) 215718.
[28] W. Li, T. Ma, T. He, Y. Li, S. Yin, Chem. Eng. J. 463 (2023) 142495.
[29] X. Wu, Y. Zhang, Y. Ding, et al., Adv. Sci. 12 (2025) 2414525.
[30] C. Dai, L. Wang, X. You, et al., Chin. Chem. Lett. 36 (2025) 109869.
[31] S. Yu, R. Zhang, Z. Xie, et al., ACS Biomater. Sci. Eng. 10 (2024) 4336–4346.
[32] J. Li, T. Wang, Y. Shi, et al., J. Nanobiotechnol. 22 (2024) 7.
[33] J. Ming, J. Zhang, Y. Shi, et al., Nanoscale 12 (2020) 3916–3930.
[34] H. Zhu, Q. Chi, Y. Zhao, et al., Mater. Res. Bull. 47 (2012) 3637–3643.
[35] Y. Liu, B. Yu, X. Dai, N. Zhao, F.J. Xu, Biomaterials 274 (2021) 120885.
[36] N. Tao, L. Jiao, H. Li, et al., ACS Nano 17 (2023) 22844–22858.
[37] X. Lan, J. Liang, C. Wen, et al., Chin. Chem. Lett. 35 (2024) 108616.
[38] C. Huang, X. Yang, Q. Yu, L. Zhang, D. Zhu, Chin. Chem. Lett. 35 (2024) 109680.
[39] P. Lan, H. Chen, Y. Guo, et al., Nano Lett. 22 (2022) 4741–4749.